Nonreciprocal Wavefront Engineering with Time-Modulated Gradient Metasurfaces

J. W. Zang[1,2], D. Correas-Serrano[1], J. T. S. Do[1], X. Liu[1], A. Alvarez-Melcon[1,3], J. S. Gomez-Diaz[1]*
[1]Department of Electrical and Computer Engineering, University of California Davis
One Shields Avenue, Kemper Hall 2039, Davis, CA 95616, USA.
[2]School of Information and Electronics, Beijing Institute of Technology, Beijing 100081, China
[3] Universidad Politécnica de Cartagena, 30202 Cartagena, Spain
*E-mail: jsgomez@ucdavis.edu

We propose a paradigm to realize nonreciprocal wavefront engineering using time-modulated gradient metasurfaces. The essential building block of these surfaces is a subwavelength unit-cell whose reflection coefficient oscillates at low frequency. We demonstrate theoretically and experimentally that such modulation permits tailoring the phase and amplitude of any desired nonlinear harmonic and determines the behavior of all other emerging fields. By appropriately adjusting the phase-delay applied to the modulation of each unit-cell, we realize time-modulated gradient metasurfaces that provide efficient conversion between two desired frequencies and enable nonreciprocity by (i) imposing drastically different phase-gradients during the up/down conversion processes; and (ii) exploiting the interplay between the generation of certain nonlinear surface and propagative waves. To demonstrate the performance and broad reach of the proposed platform, we design and analyze metasurfaces able to implement various functionalities, including beam steering and focusing, while exhibiting strong and angle-insensitive nonreciprocal responses. Our findings open a new direction in the field of gradient metasurfaces, in which wavefront control and magnetic-free nonreciprocity are locally merged to manipulate the scattered fields.

1. Introduction

Gradient metasurfaces have enabled the control of electromagnetic waves in ways unreachable with conventional materials, giving rise to arbitrary wavefront shaping in both near- and far-fields [1-6]. These surfaces are constructed using spatially-varying subwavelength resonant elements that impart inhomogeneous transverse momentum to the incoming waves and permit to manipulate the amplitude, phase, and polarization of the scattered fields. In addition, the development of Huygens-based structures composed of unit-cells that combine magnetic and electric responses has overcome the low conversion efficiency challenges found in early designs [7-11]. As a result, gradient metasurfaces have triggered the pursuit of exciting devices such as invisibility cloaks [12,13], flat lenses [14-16], absorbers [17-19], or polarization-dependent light splitters [20-22], greatly extending the responses provided by reflectarray antennas [23] and frequency-selective surfaces (FSS) [24] at micro and millimeter waves and even paving its way to the realm of nonlinear optics to tailor the generated wave-fronts at will [25-27].

Adding *temporal modulation* to gradient metasurfaces can further enrich their functionalities and enable more ambitious applications. For instance, it has been shown that spatiotemporally modulating the surface-impedance of an ultrathin layer permits overcoming geometrical symmetry constraints by inducing space-time photonic transitions that enable non-reciprocal beam-scanning [28]. In fact, simultaneously imposing space- and time- gradient phase discontinuities at the interface between two media leads to a more general form of classical Snell's relations not bounded by Lorentz reciprocity [29]. Very recently, the concept of time-modulated Huygens metasurfaces has been put forward and demonstrated at microwaves [30]. By independently time-modulating the electric and magnetic dipoles that compose each meta-atom, this approach enables dynamic control of the conversion efficiency, shape, and direction of the nonlinear harmonics generated by the metasurface upon simple plane-wave illumination. The arguably major challenges faced by this platform are (i) the complicated time-varying waveforms that need to be applied to the tunable elements of each cell to enforce an adequate overlap between electric and magnetic contributions; and (ii) the limited operational bandwidth that it exhibits. Similar time-modulated metasurfaces have also been explored considering graphene-wrapped silicon microwires as unit-cells [31]. It has theoretically been shown that controlling the signals that modulate the conductivity of each graphene tube permits to manipulate the wave-front and amplitude of the generated harmonics. It should also be noted that space-time coding has recently been applied to develop digital metasurfaces able to tailor electromagnetic waves in space and frequency [32]. Such surfaces have demonstrated beam-scanning and shaping of nonlinear harmonic frequencies with dynamic control through a field-programmable gate array (FPGA). In a related context, magnetless approaches to break reciprocity [33,34], mostly through spatiotemporal modulation [35-37] and nonlinearities [38, 39], have recently received significant attention and have led to a wide variety of devices in acoustics and electromagnetics such as circulators and isolators [40-48].

Here, we propose the concept of *nonreciprocal wavefront engineering* and explore it by appropriately modulating the reflection coefficient of the unit-cells that compose a metasurface. This concept is pictorially illustrated in Fig. 1 by considering a plane wave oscillating at f_0 that impinges onto a time-modulated metasurface. Upon reflection, the structure efficiently up-converts most energy into the first nonlinear harmonic (or intermodulation product) at f_0+f_m, f_m being the modulation frequency, shapes the generated beam, and steers it towards a desired direction. However, a wave coming towards the metasurface from that direction at f_0+f_m simply undergoes specular reflection. Strong nonreciprocity arises because the structure is unable to conform any beam at f_0. To understand the operation principle and fundamental building block of this platform, we theoretically and experimentally demonstrate at microwave frequencies that modulating the reflection coefficient of a unit-cell in a periodic

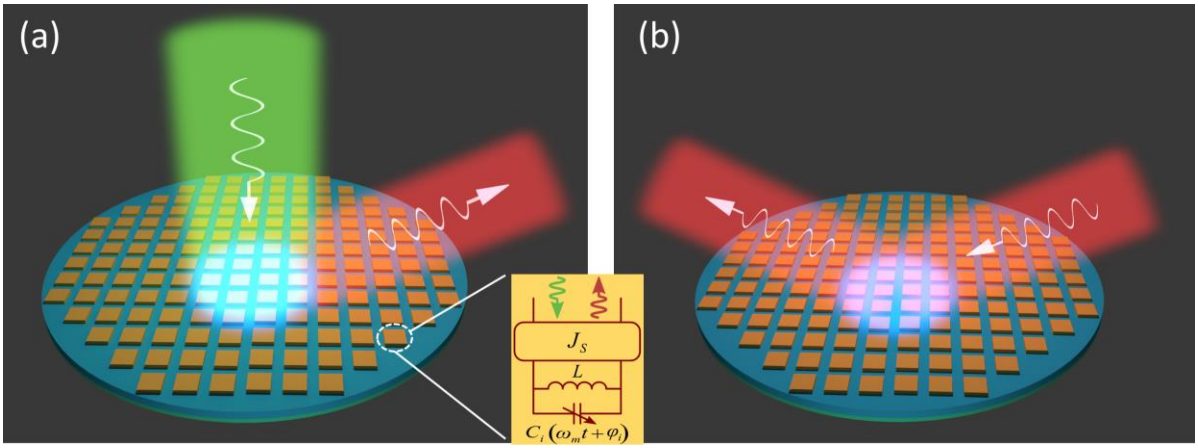

Fig. 1. Artistic representation of nonreciprocal gradient metasurfaces based on time-modulated unit-cells. Green and red waves oscillate at f_0 and $f_0 + f_m$ frequencies, respectively. The inset shows the equivalent circuit of a time-modulated unit cell.

environment allows to freely tailor the phase and amplitude of the nonlinear harmonic fields, enabling highly-efficient conversion between a pair of desired frequencies. This approach employs simple phase-delayed low-frequency tones as biasing signals and avoids the complex modulation schemes required in time-modulated Huygens metasurfaces [30]. Our proposed unit-cell operates at microwaves in the X band and elegantly separates the free-space incoming waves from biasing signals, which flow across the ground of the device through simple coplanar waveguides. We then show that nonreciprocal responses over 13 dB can be achieved by using such unit-cells, modulated with adequate phase-delayed tones, to load and terminate a rectangular waveguide. Next, we unveil the physical mechanisms that govern nonreciprocity in time-modulated metasurfaces, namely (i) the drastically different phase profiles imposed by time-modulated metasurfaces to waves oscillating at different frequencies; and (ii) the generation of nonlinear surface or propagative waves during certain up/down conversion processes. We illustrate the capabilities and broad reach of the proposed paradigm by designing and analyzing various time-modulated metasurfaces able to efficiently up-convert incoming waves to the first harmonic frequency ($f_0 \rightarrow f_0 + f_m$) and realize functionalities such as beam steering and focusing. In all cases, the metasurfaces are unable to shape any beam at the fundamental frequency ($f_0 + f_m \rightarrow f_0$) and exhibit angle-insensitive nonreciprocal responses over 20 dB. This unprecedented nonreciprocal performance goes well beyond the current state of the art, in which time-modulated techniques provide angular-dependent nonreciprocal harmonic generation and filtering [29, 31, 46]. We finalize by discussing the major opportunities and challenges faced by nonreciprocal time-modulated metasurfaces, including the development of sophisticated unit-cells and tunable phase-controlled low-frequency feeding networks. Such networks will empower time-modulated surfaces to dynamically implement arbitrary wave-fronts, combining exciting applications such as cloaking, camouflage, polarization-dependent routing, or near-field focusing with very large isolation. The proposed platform can be applied to realize tailored, nonreciprocal solutions at RF, terahertz, infrared, and optics provided that tunable components that can be modulated with low-frequency signals —such as varactors and high-quality 2D [49, 50] or optomechanical materials [51, 52]— are available. Similar concepts may be extended to enable strong nonreciprocal responses in other fields such as mechanics [53] and thermodynamics [43].

2. Theory of nonreciprocal time-modulated gradient metasurfaces

Let us consider an infinite two-dimensional array of identical unit-cells that operate in reflection and resonate at $\omega_0 = 2\pi f_0$. Each cell is tunable and thus can be characterized using a resonator composed of an inductor and a varactor that provides a tunable capacitance through a biasing voltage. The coupling between the resonator and free-space can be modelled using an admittance inverter [54], as shown in the inset of Fig. 1. In this form, the proposed cell could serve as a building block for reconfigurable gradient metasurfaces or reflectarray antennas, as previously proposed in the literature [55, 56]. Let us now apply a time varying modulating signal of frequency ($\omega_m = 2\pi f_m$) and phase (φ_m) to simultaneously control the varactor of all cells. Then, the capacitance C_i of each resonator 'i' will vary with time according to

$$C_i(t) = C_0\,[\,1 + \Delta_m \cos(\omega_m\, t + \varphi_m)], \tag{1}$$

where C_0 is the average capacitance value and $\Delta_m = \frac{\Delta C}{C_0}$, with ΔC being the maximum capacitance variation, is the modulation index ($0 < \Delta_m < 1$) controlled through the power of the modulating signal. In Appendix A, we show that reflection coefficient of this time-modulated surface can be expressed as

$$R'(\omega_0 + k\omega_m) = \sum_{n=-\infty}^{\infty} R_{(n,k)} e^{jn\omega_m t} \approx R_{(k,k)} + R_{(k+1,k)} e^{j\omega_m t} + R_{(k-1,k)} e^{-j\omega_m t}, \tag{2}$$

where $R_{(n,k)} = b(\omega_0 + n\omega_m)/a(\omega_0 + k\omega_m)$ is an inter-harmonic reflection coefficient that relates the fields of the incoming wave '$a(\omega_0 + k\omega_m)$' oscillating at frequency $\omega_0 + k\omega_m$ and the generated harmonic '$b(\omega_0 + n\omega_m)$' with frequency $\omega_0 + n\omega_m$ ($n, k \in \mathbb{Z}$). Additional details can be found in Appendix A. It should be emphasized that up and down conversion processes in time-modulated resonant unit-cells, for instance between different nonlinear harmonics n and k, are not identical, neither in phase nor in amplitude, which entails an intrinsic non-reciprocal behavior. Analyzing the time-modulated cell, the inter-harmonic reflection coefficient between two specific harmonics can be derived as

$$R_{(n,k)} \propto M_{(n,k)} e^{j(n-k)\varphi_m}, \tag{3}$$

where $M_{(n,k)} \neq M_{(k,n)}$ denote the amplitude of the nonlinear harmonic n and k, respectively. Assuming a modulation frequency significantly smaller than the operation frequency (i.e., $\omega_m \ll \omega_o$), it can easily be shown that the amplitudes for up and down conversion processes are similar (i.e., $M_{(n,k)} \approx M_{(k,n)}$). More interestingly, Eq. (3) reveals that the phase of the generated nonlinear harmonics is determined by the phase φ_m introduced in the modulation signal, being positive (negative) for up (down) conversion. As a result, it is possible to control and manipulate the phase shift of the harmonics –thus tailoring their direction and shape– with the phase of an auxiliary, low-frequency modulating signal acting on the capacitor of each resonator. Note that similar behavior of the reflection coefficient has very recently been found in specific configurations, namely modulating both electrical and magnetic dipoles of meta-atoms in Huygens metasurfaces [30] or the surface admittance of subwavelength elements in graphene-wrapped tubes [31]. Here, we demonstrate that such response can be obtained by simply modulating the capacitance of the resonant unit-cells that compose any metasurface.

Consider now the case of a 1D *time-modulated gradient metasurface* characterized by an inter-harmonic reflection coefficient $R_{(n,k)}(x) \propto e^{j(n-k)\varphi_m(x)}$. In this expression, $\varphi_m(x)$ denotes the smooth evolution of the cells' modulation signals phases versus the metasurface position along the *x*-axis. Assuming that a plane wave impinges at an angle θ_i relative to the direction normal to the metasurface, the Generalized Snell's law for reflected waves [1, 29] can be expanded to

$$k_n^{(r)} - k_k^{(i)} = \frac{d\mathrm{Arg}\left[R_{(n,k)}(x)\right]}{dx}, \tag{4}$$

where $\mathrm{Arg}[z]$ denotes the phase of the complex number z, $k_k^{(i)} = k_k sin(\theta_i)$ and $k_n^{(r)} = k_n sin(\theta_r)$ are the in-plane wave vector components of the incident and reflected waves, respectively, $k_n = \frac{\omega_o + n\omega_m}{c}$ and $k_k = \frac{\omega_o + k\omega_m}{c}$ are the free-pace wavenumbers, and $\frac{d\mathrm{Arg}[R_{(n,k)}(x)]}{dx} = (n-k)\frac{d\varphi_m(x)}{dx}$ is the additional in-plane wave number imposed to the *n* harmonic generated by the time-modulated surface. The importance of Eq. (4) is threefold. First, it shows that the sign of the phase gradient is different for up (positive) and down (negative) conversion processes. This subtle difference has very important implications for *nonreciprocal wavefront engineering*. For instance, it permits to tailor the phase-profile exhibited by time-modulated metasurfaces at a given frequency. As a result, the structure will be able to convert an incoming plane wave into a harmonic beam ($n \to k$) with tailored shape and direction. However, in the dual case ($k \to n$), the metasurface will exhibit a phase profile that is exactly the negative to the previous one. In such profile, the phase difference between two arbitrary unit-cells changes from positive to negative, which prevents any meaningful beam shaping. Furthermore, and as described in detail below, it is possible to impede the generation of *propagative* harmonic beams and obtain instead surface waves at the metasurface interface. Second, Eq. (4) explicitly shows that the wavenumbers of plane waves oscillating at different frequencies are involved in the reflection process, and therefore they should be considered in the design process. And third, it also confirms that time-modulated metasurfaces do not provide any phase-gradient when the frequencies of the incident and reflected waves are the same (i.e., $n = k$). In this case, the usual Snell's law of reflection is retrieved. These properties are in clear contrast to the ones of common linear, gradient metasurfaces, which exhibit a fixed phase profile imprinted in their subwavelength resonators. Despite their physical insight, it should be noted that the Generalized Snell's laws rely on a wave approximation corresponding to geometric optics that works well to shape beams in the far-field. The synthesis of arbitrary wavefronts, especially in the near-field, require more rigorous, full-wave, approaches [5, 57, 58].

The simplest and probably most representative example of *non-reciprocal wavefront engineering* with time-modulated metasurfaces, illustrated in Fig. 2a, consists of converting a plane wave oscillating at f_0 and coming from an angle θ_i into a beam at $f_0 + f_m$ and steering it towards an angle θ_r in free-space. In the dual case, a plane wave oscillating at $f_0 + f_m$ that impinges onto the metasurface will not generate any wave scattering or beam shaping at f_0, virtually achieving infinite isolation. Such response can be obtained by (i) achieving efficient frequency conversion between f_0 and the nonlinear harmonic at $f_0 + f_m$ while strongly limiting the energy coupled to any other intermodulation frequency, as described below; and (ii) synthesizing the phase profile of the signals that modulate the unit-cells composing the metasurface as $\frac{d\mathrm{Arg}[R_{(1,0)}(x)]}{dx} = \frac{2\pi}{\Lambda} = k_1 sin(\theta_r) - k_0 sin(\theta_i)$, where Λ is the distance along the *x*-axis of the metasurface where the phase applied to the modulating signals has changed a total of 2π radians. Numerical simulations depicted in Fig. 2b (left panel) showcase this scenario and confirm that the imposed time-modulation shapes the harmonic wave and steers it towards a desired angle. At the fundamental frequency, the beam simply undergoes specular reflection because the metasurface does not impose any additional wavenumber to the

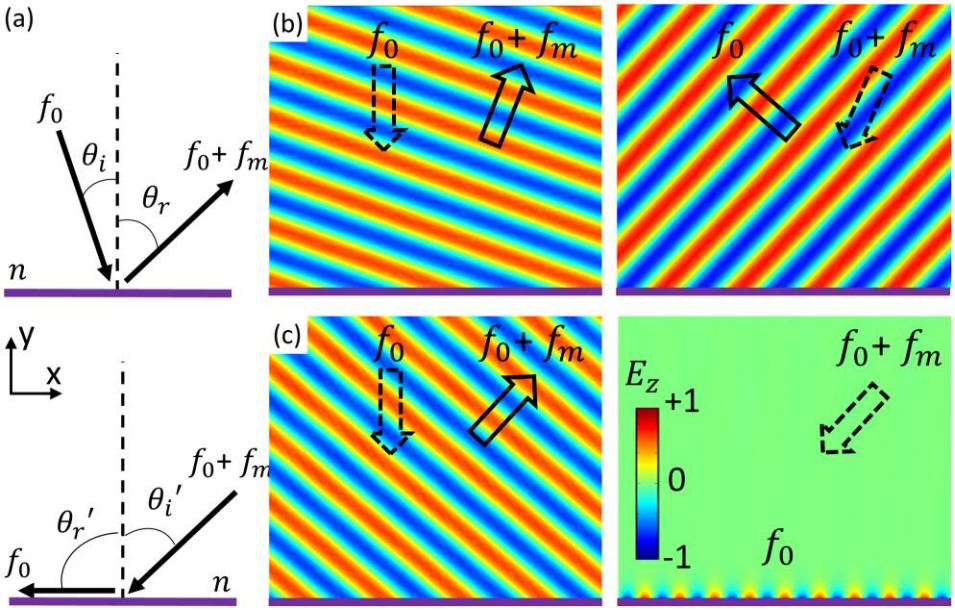

Fig. 2. (a) 1D sketch of wave reflection provided by a time-modulated metasurface (magenta) designed to up-convert a plane wave coming from the angle θ_i and oscillating at f_0 to the first nonlinear harmonic ($f_0 + f_m$) and steer it towards the direction θ_r. The schematic at the bottom illustrates the dual case: a plane wave oscillating at $f_0 + f_m$ and coming from $\theta_i' = -\theta_r$ impinges into the surface and is down-converted to f_0 and steered towards θ_r'. (b) Distribution of the z-component of the electric field oscillating at $f_0 + f_m$ scattered by a time-modulated metasurface designed for $\theta_i = 0°$ and $\theta_r = 20°$. Right panel shows the scattered fields at f_0 in the dual case, i.e., the metasurface is illuminated by a plane wave coming from $\theta_i' = 20°$ and oscillating at $f_0 + f_m$. (c) Similar as (b) but considering now a time-modulated antenna designed for $\theta_i = 0°$ and $\theta_r = 46°$. Right panel confirms the lack of scattered fields at f_0 in the dual case and the generation of surface waves. Results have been computed using COMSOL Multiphysics considering $f_0 = 8.6$ GHz and $f_m = 600$ MHz.

reflected waves, i.e., $\frac{d\text{Arg}[R_{(0,0)}(x)]}{dx} = 0$. For the $n = -1$ harmonic, the time-modulated surface imparts a phase-gradient $\frac{d\text{Arg}[R_{(-1,0)}(x)]}{dx} = -\frac{d\text{Arg}[R_{(1,0)}(x)]}{dx} = -\frac{2\pi}{\Lambda}$ that directs it towards the direction opposite to the one of the $n = +1$ harmonic. Let us now analyze the dual case (see the bottom of Fig. 2a): a plane wave oscillating at $f_0 + f_m$ impinges onto the metasurface from the direction $\theta_i' = -\theta_r$. In most cases, as the one shown in Fig. 2b (right panel), the metasurface will generate fields oscillating at f_0 that will conform a propagative plane wave. Applying Eq. (3) allows us to retrieve the direction of the reflected beam as $sin(\theta_r') = sin(\theta_i) + \frac{2\pi}{\Lambda}\left(\frac{k_1+k_0}{k_1 k_0}\right)$. This equation clearly shows that the beam is further steered towards the backfire direction as the in-plane wavenumber imparted by the metasurface $\left(\frac{2\pi}{\Lambda}\right)$ increases. In the limiting case, illustrated in Fig. 2c, the beam generated leads to surface waves that propagate along the metasurface and thus are unable to propagate back to the medium. Such situation appears when the time-modulated metasurface imposes a wavenumber

$$k_c = \frac{2\pi}{\Lambda_c} \geq \left(1 - sin(\theta_i)\right)\frac{k_1 k_0}{k_1 + k_0}. \quad (\mathbf{5})$$

Given the analogue response provided by this wavenumber and the critical angle found at the interface between two dielectric media [59], we have denoted k_c as the *critical wavenumber*. It permits the engineering of time-modulated metasurfaces with very strong nonreciprocity by exploiting the interplay between propagative and surface waves during up/down conversion processes.

In addition to the phase control of the fields emerging from time-modulated metasurfaces, *boosting and tailoring the conversion efficiency* of the process is critical to enable practical applications. In many cases, it is necessary to prevent the generation of multiple harmonics and restrict the nonlinear processes to be very efficient in the conversion between two desired nonlinear harmonics n and k associated to the frequencies of interest. One approach may be designing Huygens metasurfaces [30] and then independently modulating the electric and magnetic dipoles that compose each meta-atom. Even though this method enables large flexibility, it requires two non-linear elements per unit-cell and relatively complicated time-waveforms to properly control the cell response. Besides, losses can be significant and may hinder the use of such structures in practice. Another option could be engineering structures that simultaneously resonate at two desired frequencies, as recently realized in nonlinear gradient metasurfaces aimed for second-harmonic generation [27]. Unfortunately, such designs are challenging in time-modulated metasurfaces because (i) both tunable resonances should equally depend on the modulation signal; and (ii) the spectral separation between fundamental and harmonic signals is usually small.

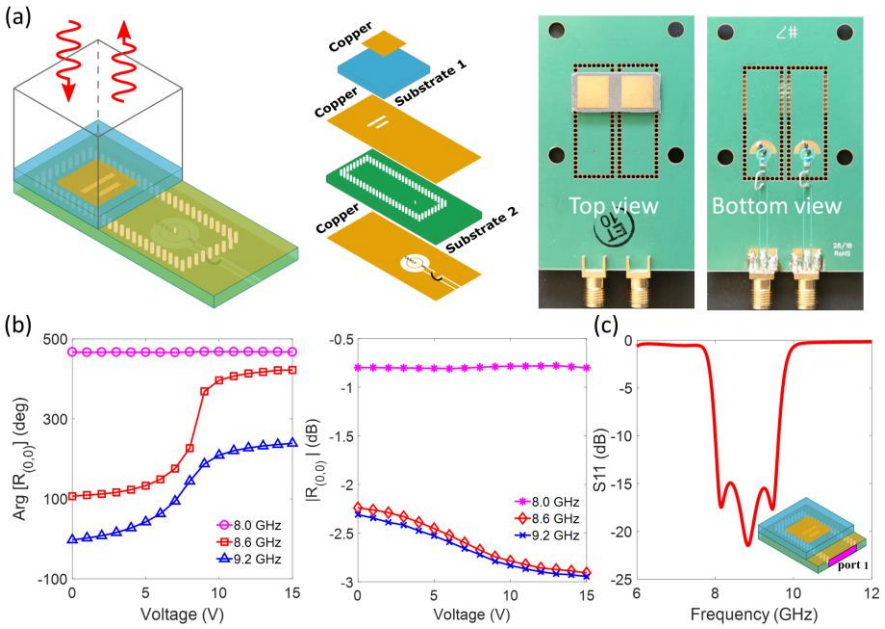

Fig. 3. (a) Proposed unit-cell based on a patch antenna coupled to a substrate integrated waveguide through two slots. The short-circuited SIW line is loaded with a shunt varactor that is biased through a coplanar waveguide located in the ground plane. Further details can be found in Appendix C. (b) Measured phase and magnitude of the unit-cell reflection coefficient. Results are obtained exciting the unit-cell from the normal direction, as shown in panel (a), and are plotted versus the varactor biasing voltage for several operation frequencies. (c) Simulated scattering parameters of the unit-cell located in an infinite periodic environment and excited from the SIW line.

3. Time-modulated unit-cells

In this Section we introduce a new unit-cell operating at microwaves that allows to efficiently modulate its reflection coefficient. The structure is designed to provide very efficient frequency-conversion between the fundamental frequency and the first nonlinear harmonic while allowing full manipulation of the phase of the emerging fields by tuning the phase of the low-frequency modulating signal. The cell is composed of a resonant patch and several resonant slots coupled to a short-circuited substrate integrated waveguide (SIW) [60] that hosts a varactor diode in shunt configuration, as illustrated in Fig. 3a. At desired frequencies, incoming waves couple to the SIW through the resonances provided by the patch and the slots, propagate along the SIW, are reflected at the short-circuit, travel back along the SIW, and are re-radiated to free-space. Note that SIW is used as simple delay line that does not interfere in the coupling between the cell and free-space. In addition, the varactor is located roughly $\lambda/4$ away from the SIW short-circuit to implement a tunable resonator. Physically, this lumped component is placed in the backside of the SIW through a via-hole and is biased using a coplanar waveguide. The capacitance provided by the varactor together with the short circuit of the SIW line implement the resonator shown in the inset of Fig. 1. Feeding the coplanar waveguide with a tone permits to easily time-modulate such resonator while preventing unwanted coupling between the incoming energy and the modulation signal. Fig. 3b shows the measured phase $\left(\text{Arg}\left[R_{(0,0)}(\omega)\right]\right)$ and magnitude $\left(\left|R_{(0,0)}(\omega)\right|\right)$ of the unit-cell reflection coefficient versus the static biasing voltage of the varactor. Results confirm that, in the absence of time-modulation, the cell provides a phase range over $300°$ at several frequencies thus assuring that it can host efficient frequency conversion processes. Besides, it confirms that the loss introduced by the cell is low, remaining below 3 dB in all cases. Numerical simulations shown in Fig. 3c reveal a relatively broadband (≈19%) coupling to free-space from the SIW line. The resulting sharp transfer function, obtained after a proper adjustment of the couplings between the slots and the patch, helps attenuating unwanted harmonics generated by the varactor.

In order to test the response of the unit-cell upon time-modulation in a controlled environment, we have placed it within an infinite waveguide simulator [23]. This configuration has widely been employed in the fields of reflectarrays and phased-array antennas [61] and exploits the fact that, under certain conditions, a common rectangular waveguide loaded with unit-cells exactly reproduces the behavior of a transverse electric (TE) plane wave propagating in free-space that impinges onto an infinite array of unit-cells with a given angle with respect to the direction normal to the structure. In our case, the required conditions are fulfilled by using two symmetric unit-cells with identical time-modulation. The experimental set-up employed to test our proposed unit-cell is shown in Fig. 4a (see Appendix C for further details). Specifically, we use a source to generate a low-frequency signal $f_m = 600$ MHz and a phase-shifter to control its phase (φ_m). Note that the signal amplitude controls the modulation index Δ_m. In addition, we employ a directional coupler to direct the microwave signal oscillating at $f_0 = 8.6$ GHz to the waveguide simulator and to couple the reflected signals to a spectrum or a vector network analyzer. Here, we define loss as the ratio between the power generated at the harmonic of interest and the power from the generator (see Appendix C for a description of the calibration scheme), and conversion efficiency as the power ratio between two desired frequencies. Fig. 4b shows the measured phase of the inter-harmonic reflection coefficients $\text{Arg}\left[R_{(1,0)}\right]$ and $\text{Arg}\left[R_{(0,1)}\right]$ versus the phase of the

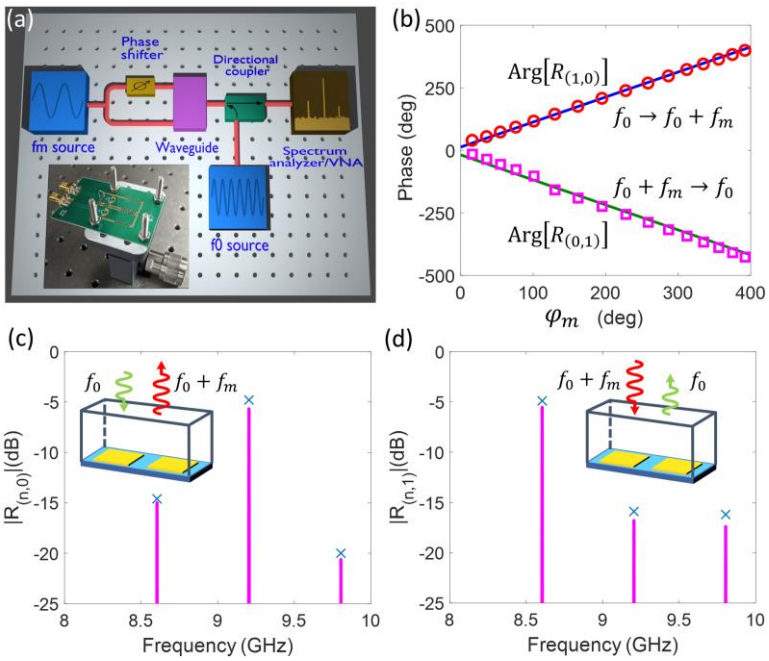

Fig. 4. (a) Experimental set-up employed to characterize time-modulated unit-cells within an infinite waveguide simulator [23]. The cells are simultaneously modulated with a harmonic signal with frequency $f_m = 600$ MHz, modulation index $\Delta_m = 0.05$, and phase φ_m. The inset shows a picture of two cells in a WR90 waveguide flange. This scenario is equivalent to an infinite array of unit-cells placed in free-space and excited by a TE plane wave. (b) Measured (markers) and numerically simulated (solid line) phase of the inter-harmonic reflection coefficient $\text{Arg}[R_{(1,0)}]$ and $\text{Arg}[R_{(0,1)}]$ versus the phase of the modulating signal φ_m. (c)-(d) Measured (solid line) and simulated (markers) amplitude of the reflected waves when the waveguide is excited at $f_0 = 8.6$ GHz and $f_0 + f_m = 9.2$ GHz, respectively. Additional details of the experimental set-up are provided in Appendix C.

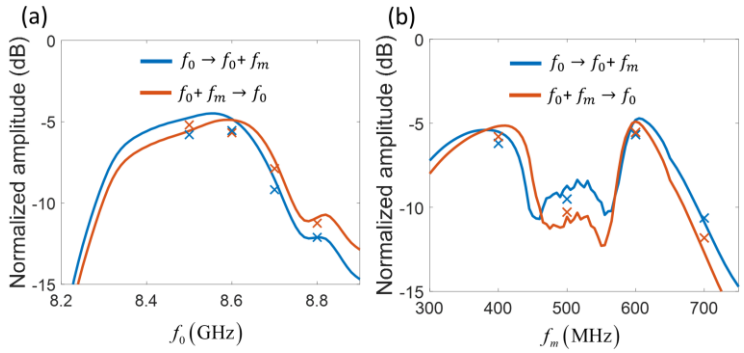

Fig. 5. Normalized amplitude of the generated harmonics for up ($f_0 \rightarrow f_0 + f_m$, blue) and down ($f_0 + f_m \rightarrow f_0$, orange) conversion processes in the unit-cell described in Fig. 3. The set-up follows the one described in Fig. 4a. Results, computed using numerical simulations (solid lines) and with experiments (markers), are plotted versus (a) operation frequency f_0, keeping $f_m = 600$ MHz; and (b) modulation frequency f_m, keeping $f_0 = 8.6$ GHz. Other parameters are as in Fig. 4.

modulating signal φ_m. Results show the linear dependence between the different phases and confirm the positive/negative slope for up-conversion (0→1)/ down-conversion (1→0), experimentally demonstrating nonreciprocity in phase. The measured data also confirms that the proposed unit-cell can tailor the phase of the emerging fields over a wide range, which is crucial to enable beam-shaping functionalities. Figs. 4c-d show the measured amplitude of the signals generated by the cells when excited at the fundamental f_0 frequency and the first harmonic $f_0 + f_m$, respectively. Results show symmetrical conversion efficiencies over 10 dBs for both up and down processes, with a loss of the overall process of 5 dB (around 72.5 % in linear scale). We emphasize that such loss is well within the range of state of the art of reconfigurable metasurfaces and reflectarrays [56]. Remarkably, the generation of unwanted harmonics has been significantly mitigated thanks to the sharp frequency-dependent coupling between the cell and free-space (see Fig. 3c). Fig. 5a explores the bandwidth of the unit-cell by showing the normalized amplitude (see Appendix C) of the generated harmonics for up ($f_0 \rightarrow f_0 + f_m$) and down ($f_0 + f_m \rightarrow f_0$) conversion processes versus f_0. Results confirm that a bandwidth over 300 MHz is achievable with a loss below 7.5 dB. Besides, Fig. 5b shows the normalize amplitude versus the modulation frequency f_m, confirming that other time-modulation schemes can be applied to the cell while maintaining low loss. Our study confirms that the proposed time-modulated unit-cell can tailor the phase of the generated harmonics, achieve very good conversion efficiency between two desired frequencies, and provide an operational bandwidth of 300 MHz. The potential applications of this cell extend beyond the context of nonreciprocity explored here and

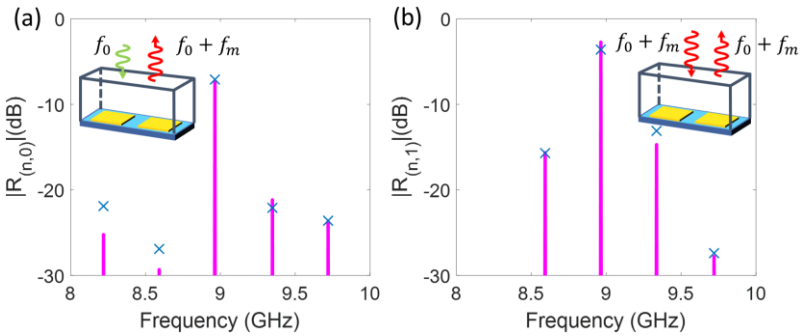

Fig. 6. Measured (solid line) and simulated (markers) normalized amplitude of the waves reflected on a waveguide terminated with two time-modulated unit-cells. The measurement set-up follows the one described in Fig. 4a. The cells are biased with harmonic signals that oscillate at $f_m = 370$ MHz and exhibit a phase difference of $\varphi_d = 130°$. The excitation frequency employed in panels (a) and (b) is $f_0 =$ 8.6 GHz and $f_0 + f_m = 8.97$ GHz, respectively. Modulation index is set to $\Delta_m = 0.05$. Additional details of the experimental set-up are provided in Appendix C.

include the development of gradient metasurfaces aimed at arbitrary wave-shaping, true-time delay configurations able to exploit the large phase range that the cell provides, as well as more specific applications in the fields of reflectarray antennas and lenses.

Aiming to investigate the ability of the proposed cells to impart phase-gradients through time-modulation, we study their electromagnetic response within the waveguide simulator when the varactors are biased with modulating signals that oscillate at the same frequency $f_m = 370$ MHz but exhibit different phases, φ_{m1} and φ_{m2}. It should be noted that, in contrast to the previous example, this case does not directly correspond to an infinite array of unit-cells located in free-space but simply to a waveguide terminated with a time-modulated load. We employ this example to demonstrate that nonreciprocity in amplitude can indeed be achieved with this cell, even though it has not been optimized for such operation. Fig. 6 shows the measured amplitude of the reflected signals when the phase difference between the modulation signals is $\varphi_{md} = \varphi_{m1} - \varphi_{m2} = 130°$. Exciting the time-modulated load through the waveguide at the fundamental frequency $f_0 = 8.6$ GHz efficiently up-converts (>20 dB) the incoming energy to the first harmonic $f_0 + f_m$=8.97 GHz whereas very little power is transferred to other harmonics, as shown in Fig. 6a. The first nonlinear harmonic becomes dominant, exhibiting over 13 dB more power than any other intermodulation product. The overall loss is 7.3 dB (81 % in linear scale), which is 2.3 dB larger than the one provided by the cell in the absence of time-induced phase-gradients. The loss increase is due to the excitation of surface waves on the cells. In the dual case, depicted in Fig. 6b, the load is excited at $f_0 + f_m$= 8.97 GHz and most of the reflected power remains at this frequency without undergoing any frequency conversion. The phase-gradient imparted by the time-modulated load prevents any energy scattering at f_0 and forces the energy to remain at the excitation frequency within the SIW line, from where it is subsequently radiated back towards the waveguide. Such mechanism decreases the influence of loss to 2.4 dB (46.7% in linear scale) and forces the excitation frequency $f_0 + f_m$ to become dominant, with over 13 dB more power than other harmonics. This example clearly illustrates how phase-gradients imposed by time-modulated cells are useful to engineer and induce strong non-reciprocal responses.

It should be noted that the proposed unit-cell is optimized for nonreciprocal operation between two desired frequencies. Compared to the recently introduced Huygens' cells for parametric waves [30], which are composed of tunable electric and magnetic dipoles, this multilayer design only requires one tuning element per unit-cell that is time-modulated with a simple low-frequency tone. This scheme avoids the challenge of determining intricated modulation signals to balance and tailor the electric and magnetic contributions of the cells. In addition, note that Huygens' cells are relatively narrowband because frequency conversion process must occur within the bandwidth of their single resonance to ensure high conversion efficiency (e.g., time-modulated signals oscillating at 2 MHz were employed in [30] for an operation frequency around 3.65 GHz). In the proposed cell, the coupling between the slots and the patch significantly enhance the static bandwidth up to 20% (see Fig. 3c) thus allowing to use larger modulation frequencies that improve the operational bandwidth of the nonreciprocal metasurfaces.

4. Nonreciprocal beam steering and focusing with time-modulated metasurfaces

The proposed unit-cell can serve as a building block to construct time-modulated metasurfaces exhibiting exciting nonreciprocal responses. In the analysis/design process of such devices we will assume that (i) each time-modulated unit-cell is within a perfect periodic environment, which allows to take into account the coupling between adjacent cells and higher order interactions (see Fig. 4); and (ii) the variation of the modulation signals phase profile $\varphi_m(x, y)$ applied to adjacent unit-cells is smooth. These assumptions are similar to the ones usually applied in the fields of gradient metasurfaces and reflectarray antennas and therefore permit us to borrow well-established analysis and design tools employed there [23]. We note that such techniques are an approximation that works very well in practice and are systematically used to design many devices and antennas. More challenging, arbitrary wavefronts can be synthesized using full-wave approaches [5, 57,58]. In the following, we apply the measured response of the unit-cell shown in Fig. 4 (both in phase and amplitude) to numerically design and investigate time-modulated metasurfaces able to provide nonreciprocal beam steering and focusing. It should be emphasized

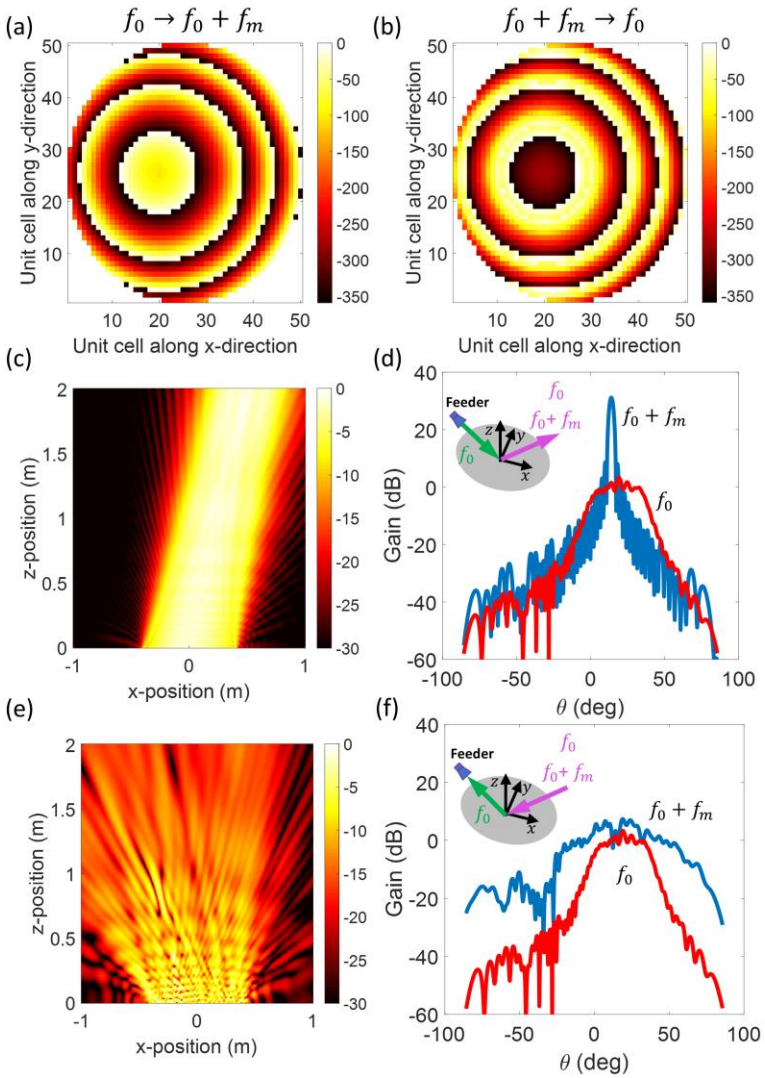

Fig. 7. Nonreciprocal beam shaping with time-modulated metasurfaces. The surface is composed of 50x50 unit-cells (as the one described in Fig. 4) designed to up-convert incoming waves oscillating at f_0 to the first harmonic, $f_0 + f_m$, and direct the generated beam towards the direction $\theta_0 = 14°, \varphi_0 = 0°$. The feeder is an *x*-polarized horn antenna located at $x_F = -322$mm, $y_F = 0$mm, and $z_F = 838$mm with respect to the surface center. (a)-(b) Phase (in degrees) profile imparted by the time-modulated metasurface for up ($f_0 \rightarrow f_0 + f_m$) and down ($f_0 + f_m \rightarrow f_0$) conversion processes, respectively. Panels (c) and (d) show the up-conversion response of the metasurface when excited at f_0 from the feeder. (c) Normalized power density (dB) of the waves oscillating at $f_0 + f_m$ generated by the metasurface. (d) Up-conversion radiation diagram. Panels (e) and (f) show the down-conversion response of the metasurface. (e) Normalized power density (dB) of the waves oscillating at f_0 generated by the metasurface when excited by a plane wave at $f_0 + f_m$ coming from $\theta_0 = 14°, \varphi_0 = 0°$. (f) Far-field distribution that, upon reflection on the time-modulated metasurface, would focus on the feeder at f_0. Panels (c) and (e) have been normalized to the same power level.

that the unit-cells that compose the resulting metasurfaces are identical and time-modulated using a modulation frequency $f_m = 600$ MHz and a modulation index of $\Delta_m = \frac{\Delta C}{C_0} \approx 0.05$ (see Eq. (1)). The desired functionalities are realized by adequately tailoring the phases of the modulation signals that control the different unit-cells.

As a first example, we design a time-modulated metasurface composed of 50x50 unit cells able to shape a TE plane wave oscillating at $f_0 + f_m = 9.2$ GHz towards the direction $\theta_0 = 14°, \varphi_0 = 0°$. The separation distance between cells is 16.7 mm, which is below half wavelength at the design frequency. The surface is illuminated using an *x*-polarized horn antenna (modeled with a $cos^q(\theta)$ function, with $q = 10$ [23]) transmitting at $f_0 = 8.6$ GHz and located at the position $x_F = -322$ mm, $y_F = 0$ mm, and $z_F = 838$ mm with respect to the center of the surface. Figs. 7a-b show the phase profile imparted by the time-modulated surface for up ($f_0 \rightarrow f_0 + f_m$) and down ($f_0 + f_m \rightarrow f_0$) conversion processes, respectively. It is evident that they exhibit sharp differences. The phase-profile for up-conversion has specifically been designed using the information from Fig. 4b to achieve the desired performance. In contrast, in the down-conversion process, each time-modulated unit-cell provides a negative phase-shift with respect to the up-conversion case that prevents any control over the generated beam. In addition, some cells may impart a momentum larger than the critical one, thus partially preventing energy scattering at f_0. From the practical

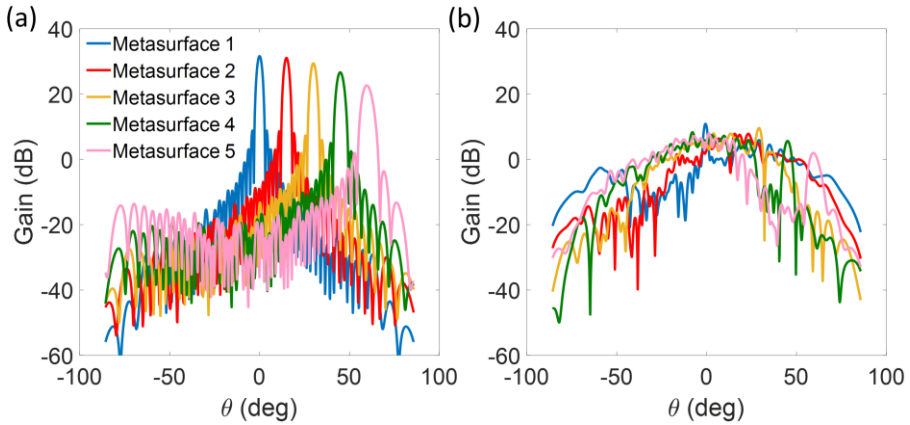

Fig. 8. Several time-modulated metasurfaces (as the one described in Fig. 6) designed to up-convert waves oscillating at f_0 coming from the feeder into the first nonlinear harmonic, $f_0 + f_m$, and steer the generated beam towards the directions $\theta_0 = [0°, 15°, 30°, 45°, 60°]$, respectively, with $\varphi_0 = 0°$. (a) Far-field distribution oscillating at $f_0 + f_m$ shaped by the metasurfaces excited by the feeder at f_0. (b) Far-field distribution oscillating at $f_0 + f_m$ that, upon reflection on the time-modulated metasurface, would focus on the feeder at f_0.

point of view, the phase difference among the modulation signals that control the metasurface unit-cells can readily be obtained from Fig. 7b. Fig. 7c illustrates the power density of the beam shaped by the metasurface at $f_0 + f_m$ in the plane y=0, confirming that it is indeed directed towards the desired direction. The up-conversion far-field diagram of the metasurface is depicted in Fig. 7d. Results show that a high gain beam (26.8 dB) has been obtained. In the same panel, we have also plotted the fields reflected at f_0. As discussed above, the time-modulated metasurface does not provide any extra phase to waves that remain at the same frequency as the coming ones, and therefore the structure simply behaves as a lossy specular reflector unable to shape the wavefront. Let us now examine the dual case: a plane wave oscillating at $f_0 + f_m$ impinges on the metasurface from the direction $\theta_0 = 14°, \varphi_0 = 0°$. Upon reflection, the structure efficiently down-converts the waves to f_0 but, due to the negative phase-profile that it imposes, is neither able to focus the energy into the feeder nor to conform any beam (see Fig. 7e). We note that a reciprocal surface would have focused the beam into the feeder. To determine the spatial distribution of plane waves oscillating at $f_0 + f_m$ that after reflection on the surface would have been focused into the feeder at f_0, i.e., the down-conversion radiation diagram, we trace back the path followed by such waves. To do so, we simply analyze the response of the metasurface operating in down-conversion (i.e., $f_0 + f_m \rightarrow f_0$) when it is excited from the feeder at f_0. Once the radiation patterns for up and down conversion have been retrieved, the nonreciprocal behavior of the metasurface is obtained by analyzing the differences between both patterns. Fig. 7f depicts the down-conversion radiation diagram of the time-modulated surface. Results show that a spatially broad distribution of plane waves oscillating at $f_0 + f_m$ simultaneously illuminating the metasurface is required to focus the energy (at f_0) on the feeder position. Such response clearly indicates that the metasurface is unable to shape any beam during down-conversion processes. Instead, it incoherently distributes the generated power in space. Strikingly, even a simple piece of metal with identical size as the metasurface exhibits better beam-shaping capabilities. A comparison between Figs. 7d and 7f unveils large nonreciprocity, over 20 dB. The reported nonreciprocity is robust, angle-insensitive, and is preserved in all beam-shaping scenarios due to the strong difference between the phases-profile in up/down conversions processes. To show that this is indeed the case, we have designed time-modulated metasurfaces able to direct the beam at $f_0 + f_m$ towards different pointing angles, ranging from $\theta_0 = 0°$ to $70°$ (in steps of one degree) keeping in all cases $\varphi_0 = 0°$. Such responses can be achieved in practice on a single metasurface by adjusting the modulation phase profile $\varphi_m(x, y)$ applied to the biasing signals using a FPGA [32]. Some of the up/down radiation diagrams of the metasurface designs are depicted in Fig. 8. Our numerical results demonstrate again the inability of the surface to tailor any beam in the down conversion process, leading in all cases to similarly uncollimated broad patterns. As consequence, the nonreciprocal strength of the surface is mostly determined by the maximum gain achieved in the up-conversion process.

As a second example, we adequately tailor the phases of the signals that modulate the metasurface described above to down-convert a TE plane wave coming from $\theta_0 = 30°, \varphi_0 = 0°$ with frequency $f_0 + f_m$ to the $n = -1$ harmonic (i.e., f_0) and then focus it at (x_F, y_F, z_F)= $(-197,0,737)$ mm. Figs. 9a-b illustrate the phase profiles exhibited by the metasurface for the up and down conversion processes, respectively. The down-conversion phase-profile has been specifically tailored to realize the desired functionality [2] whereas the up-conversion profile has been left as an afterthought. Fig. 9c-d shows the normalized power density in the plane y=0 generated by the metasurface at f_0 and $f_0 + f_m$, respectively. Results indicate that near perfect focusing of the beam generated at f_0 has been achieved. On the contrary, the waves that remain at $f_0 + f_m$ simply undergo specular reflection on the surface and thus are not focused. To investigate the nonreciprocal response of this time-modulated metasurface, we excite it with an isotropic emitter that is located at the focus position and radiates at f_0. Fig. 9e depicts the normalized power density at $f_0 + f_m$ in the plane y=0, confirming that the surface is unable to collimate any beam. Instead, it incoherently distributes the generated energy. A reciprocal surface would have reflected a plane wave directed towards $\theta_0 =$

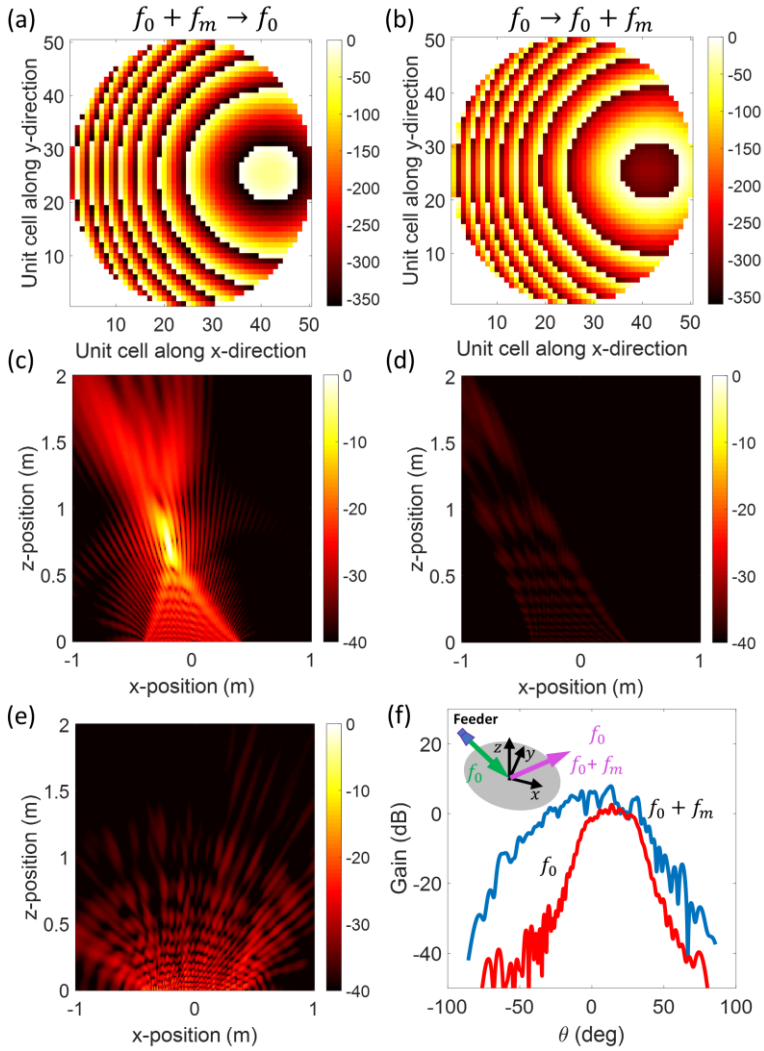

Fig. 9. Non-reciprocal focusing with time-modulated metasurfaces. The metasurface is similar to the one described in Fig. 6 but is time-modulated to down-convert a plane wave with frequency $f_0 + f_m$ and coming from $\theta_0 = 30°, \varphi_0 = 0°$ to f_0 and then focus it at (x_F, y_F, z_F)= $(-197,0,737)$ mm. (a)-(b) Phase profile (in degrees) imparted by the time-modulated metasurface for down ($f_0 + f_m \rightarrow f_0$) and up ($f_0 \rightarrow f_0 + f_m$) conversion processes, respectively. (c) Normalized power density (dB) of waves oscillating at f_0 generated by the metasurface in the plane y=0. (d) Similar as (c) but for waves oscillating at f_0+f_m. Panels (e) and (f) shows the up-conversion response of the metasurface. (e) Power density in dB of the waves oscillating at $f_0 + f_m$ generated by the metasurface when excited by an isotropic emitter radiating at f_0 and located at the focus position. (f) Up-conversion radiation diagram. Panels (c), (d) and (e) have been normalized to the same power level.

$+30°, \varphi_0 = 0°$. Finally, Fig. 9f shows the up-conversion radiation diagram of the metasurface, illustrating the inability of the surface to conform any beam.

We have established here the foundation for nonreciprocal wavefront engineering using time-modulated metasurfaces through two specific examples. The core physics that govern these devices are quite general and we expect that a much wider range of nonreciprocal time-modulated metasurfaces exhibiting advanced functionalities, including polarization control and conversion, will be investigated and demonstrated in the near future. This task will require the development of refined full-wave approaches able to accurately design surfaces that provide nonreciprocal arbitrary wavefronts, especially in the very near field. Even though we have focused this work to metasurfaces operating in reflection, our proposed platform is also perfectly suited to operate in transmission by simple time-modulating the transmission coefficient of the unit-cells. The two major challenges faced by this platform are related to the complexity of the required cells and tunable feeding networks. The former is undoubtedly the most critical aspect, since time-modulated cells should exhibit stringent responses in terms of low-loss, large and controlled tunability, bandwidth, as well as good conversion efficiency between two desired frequencies. We expect that future time-modulated cells will significantly benefit from the vibrant ongoing activity in the fields of reconfigurable gradient metasurfaces and reflectarray/lens antennas [55, 56]. On the other hand, advanced concepts and designs from the well-established field of phased-array antennas [62] can readily be translated to design low-frequency phase-agile feeding networks for the biasing signals. For instance, the responses shown in Figs. 7-9 can be obtained using a unique metasurface with a feeding network able to control the phase of signals that modulate each of the $50 \times 50 = 2500$ identical unit-cells. Even though the presence of such

network certainly increases the complexity of the structure, it can easily be printed on the metasurface ground plane using standard coplanar waveguides. Besides, note that modulation signals oscillate at relatively low-frequency (600 MHz in the examples considered in this work) which simplifies the feeding lines and permits taking advantage of low-loss, integrated, and affordable electronically controlled phase-shifters. The resulting metasurface will be able to conform quasi-arbitrary wavefronts in the low microsecond range (see Appendix C) while exhibiting very large nonreciprocal responses. Besides, simpler feeding networks can be constructed finding symmetries in the phases that should be imposed on some unit-cells to implement specific responses, as usually done in the field of phased-array antennas [62]. This vast landscape of possibilities combined with the exciting functionalities and applications enabled by time-modulated metasurfaces conforms an exciting and promising future for this technology.

5. Conclusions

Time-modulated gradient metasurfaces form an ideal platform to realize nonreciprocal wavefront engineering across the electromagnetic spectrum. This platform combines the flexibility of gradient metasurfaces to control electromagnetic waves in unique and unprecedent ways with strong and angle-insensitive nonreciprocity. To realize such devices, we proposed to modulate the reflection coefficient of the unit-cells that compose the metasurface with phase-delayed low-frequency tones. We have theoretically and experimentally shown that such modulation permits to manipulate the phase and amplitude of one desired nonlinear harmonic while fixing the field distribution of the other harmonics. Specifically, we have introduced a novel unit-cell operating at microwaves in the X band that provides efficient conversion between two desired frequencies and allows an effective modulation of its reflection coefficient. We have measured nonreciprocal responses of around 13 dB by modulating these cells with an adequate temporal phase gradient and using them to load and terminate a waveguide. In a controlled periodic environment, we characterized the cells upon time-modulation and we experimentally demonstrated a total control of the phase of the generated nonlinear harmonic in a nonreciprocal manner through the phase of the biasing signal. Appropriately extending and manipulating such phase control over the cells that compose a metasurface has allowed us to engineer nonreciprocal responses in amplitude by (i) providing drastically different phase-profile in up/down conversion between two harmonics; and (ii) exploiting the generation of propagative or surface waves in certain scenarios. The reported nonreciprocity is strong, angle-insensitive and preserved in any beam shaping scenario. Even though we have limited our analysis in this paper to functionalities like nonreciprocal beam shaping and focusing, the versatility and far-reaching implications of this platform should be emphasized: it can in principle be employed to generate arbitrary wavefronts, enable near-field light matter interactions, and realize components such as antennas, invisibility cloaks, or absorbers while simultaneously providing large nonreciprocal behavior. We envision that this paradigm will lead to a new generation of nonreciprocal devices and surfaces with wide implications in communication and sensing systems as well as in optical networks and thermal management.

Acknowledgement

This work was supported by the National Science Foundation with CAREER Grant No. ECCS-1749177. A. Alvarez-Melcon acknowledges support from grant PRX18/00092 of MECD, Spain. Authors wish to thank Prof. Eduardo Carrasco (Technical University of Madrid, Spain) for fruitful discussions, the Davis Millimeter Wave Research Center (https://www.ece.ucdavis.edu/dmrc/) for permitting access to Microwave equipment, and Roger Rogers Corporation for the generous donation of the dielectrics employed in this work.

Appendix A
Nonreciprocal response of time-modulated unit-cells

In order to analyze the time-modulated unit-cells shown in Fig. 3, we decompose the problem into two different parts. The first one is related to the linear coupling between the waves coming from free-space and the SIW of the unit-cells. Such coupling, determined by the geometry of the patch/slots and the substrates employed, behaves as a bandpass filter and is obtained using linear numerical full-wave simulations from commercial software (see Fig. 3c). These simulations are incorporated in our model using standard admittance parameters. The second part is related to the nonlinear process that occurs within the SIW. We develop in this Appendix a rigorous approach to characterize it.

In the absence of time-modulation, the unit-cell shown in Fig. 3 can be modelled using the equivalent circuit depicted in Fig. A1a. In the circuit, the "coupling" part determines how waves coming from free-space are coupled to the SIW line of the unit-cell. As mentioned above, we use linear full-wave simulations to obtain such linear coupling. The "Unit-cell: SIW" part models how the energy propagates through the SIW. Within this line, the varactor and the SIW short-circuit conform a resonator that is characterized in the circuit using an LC tank. Applying Kirchoff's current law to the nodes of the network permits to derive the following linear system of equations

$$\boldsymbol{I}_S = \left[\overline{\boldsymbol{G}}_S + \overline{\boldsymbol{Y}}_{inv} + \overline{\boldsymbol{Y}}_p\right] \cdot \boldsymbol{V}\,, \tag{A1}$$

where $\boldsymbol{I}_S = (I_s \quad 0)'$ and $\overline{\boldsymbol{G}}_S = (G_s \quad 0; 0 \quad 0)$ represent the Norton equivalent of the patch/slots and model the excitation of the SIW line, being $'$ the matrix transpose; $\overline{\boldsymbol{Y}}_{inv} = (0 \quad j\mathrm{J}_s; j\mathrm{J}_s \quad 0)$ expresses the coupling between the SIW line and the resonator using an admittance inverter; and $\overline{\boldsymbol{Y}}_p = \begin{pmatrix} 0 & 0; 0 & Y_p \end{pmatrix}$ contains the admittance of the resonator, with $Y_p = j\omega L + \frac{1}{j\omega C}$;

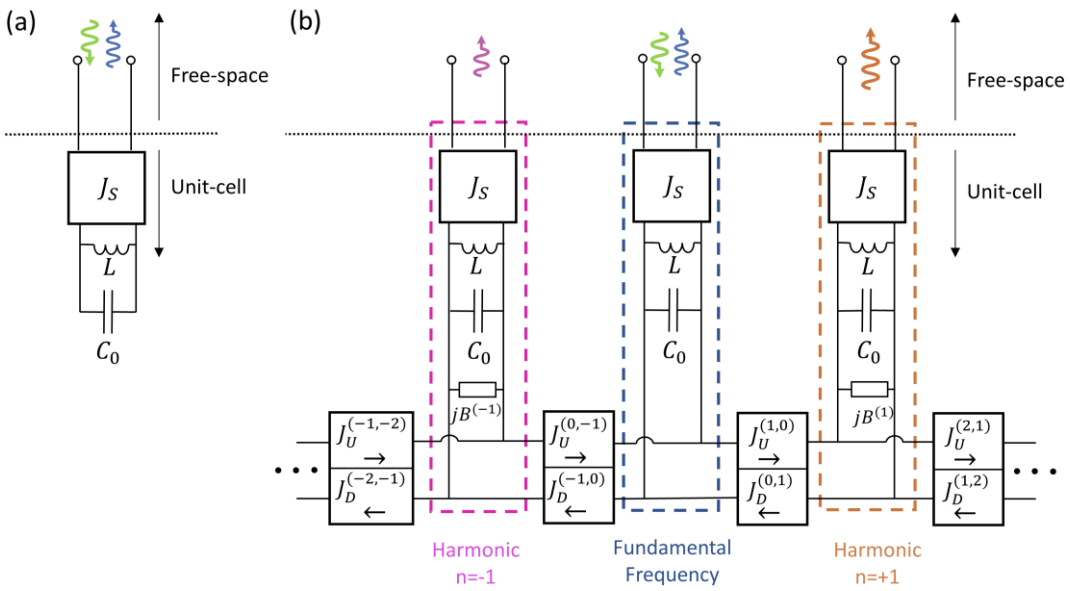

Fig. A1. Equivalent circuit of the unit-cell shown in Fig. 3 placed in a periodic environment and excited from free-space at the fundamental frequency. The "coupling" section of the circuit models how waves coming from free-space are coupled to the SIW line through the patch and slots. Such coupling is obtained using linear full-wave simulations. The "Unit-cell: SIW" part represents wave propagation within the SIW. In the line, the via-hole loaded with a varactor together with the SIW short-circuit (see Fig. 3) conforms a resonator that is characterized with an LC tank. The admittance inverter J_S models the coupling between the resonator and the SIW line. (a) Equivalent circuit in the absence of time-modulation. (b) Equivalent circuit of the unit-cell when the capacitance of the resonator is time-modulated following the scheme shown in Eq. (1). The time-modulation generates nonlinear harmonics that can couple among themselves and may radiate towards free-space. Each branch of the network, enclosed by a dashed rectangle, shows the electrical response of a given harmonic. The nonreciprocal coupling between harmonics is modelled using admittance inverters, clearly identifying up (J_U) and down (J_D) conversion, as detailed in Eq. (A7).

and $\boldsymbol{V} = (V_s \quad V_1)'$ showing the voltages in the network. We do stress that this notation based on admittance parameters is rigorous and that no approximation has been made so far. The reflection coefficient can then be retrieved analyzing this network and applying simple conversion formulas between the admittance and scattering parameters [54]. Even though this formalism does not seem the most appropriate to analyze this linear structure, it will provide useful physical insight when adding temporal modulation into the picture.

Let us now apply a time varying modulating signal to the varactors of all unit-cells that compose the metasurface as described in Eq. (1). On each cell, the time-modulation of the capacitor generates nonlinear harmonics that couple among themselves following the equivalent circuit shown in Fig. A1b. Specifically, each branch of the network represents the electrical response of a given harmonic. One side of these branches is connected to a port that models the radiation of the harmonic through the filter towards free-space whereas the other shows the internal coupling among adjacent harmonics and the fundamental frequency. The difference in the resonant frequency of each harmonic is taken into account using the susceptance

$$B^{(k)} = C_0 k\omega_m + \frac{k\omega_m}{\omega_0^2 L} \quad , \tag{A2}$$

where k denotes the harmonic order and ω_0 is the unit-cell resonant frequency in the absence of modulation. Applying Kirchoff's current law to this network and restricting the number of harmonics to N_h leads to a linear system very similar to Eq. (A1). However, each element of the matrix now becomes a submatrix of size $N_h \times N_h$, as

$$\begin{pmatrix} \boldsymbol{I_S} \\ \boldsymbol{0} \end{pmatrix} = \left[\begin{pmatrix} \bar{\boldsymbol{G}}_S & \bar{\boldsymbol{0}} \\ \bar{\boldsymbol{0}} & \bar{\boldsymbol{0}} \end{pmatrix} + \begin{pmatrix} \bar{\boldsymbol{0}} & j\bar{\mathbf{J}}_s \\ j\bar{\mathbf{J}}_s & \bar{\boldsymbol{0}} \end{pmatrix} + \begin{pmatrix} \bar{\boldsymbol{0}} & \bar{\boldsymbol{0}} \\ \bar{\boldsymbol{0}} & \bar{\boldsymbol{Y}}_{\boldsymbol{p}} \end{pmatrix} \right] \cdot \begin{pmatrix} \boldsymbol{V_S} \\ \boldsymbol{0} \end{pmatrix}, \tag{A3}$$

where $\boldsymbol{0}$ and $\bar{\boldsymbol{0}}$ are the zero vector and matrix, respectively, $\bar{\boldsymbol{G}}_S = G_s\bar{\boldsymbol{T}}$, $\bar{\mathbf{J}}_s = J_s\bar{\boldsymbol{T}}$, being $\bar{\boldsymbol{T}}$ the identity matrix, and $\boldsymbol{I}_S = (\cdots \quad 0 \quad I_s \quad 0 \quad \cdots)'$ represents the structure of the excitation vector at the fundamental frequency. Rooted in the theory reported in [63] and applying tedious but straightforward algebraic operations, the admittance submatrix of a resonator with a time-modulated capacitor including all potential couplings between the different harmonics can be derived as

$$\overline{\mathbf{Y}}_p = \begin{pmatrix} \ddots & \vdots & \vdots & \vdots & \vdots & \vdots & \vdots & \vdots & \iddots \\ \cdots & Y_r^{(-3)} & jD(\omega-2\omega_m) & 0 & 0 & 0 & 0 & 0 & \cdots \\ \cdots & jE(\omega-3\omega_m) & Y_r^{(-2)} & jD(\omega-\omega_m) & 0 & 0 & 0 & 0 & \cdots \\ \cdots & 0 & jE(\omega-2\omega_m) & Y_r^{(-1)} & jD\omega & 0 & 0 & 0 & \cdots \\ \cdots & 0 & 0 & jE(\omega-\omega_m) & Y_r^{(0)} & jD(\omega+\omega_m) & 0 & 0 & \cdots \\ \cdots & 0 & 0 & 0 & jE\omega & Y_r^{(+1)} & jD(\omega+2\omega_m) & 0 & \cdots \\ \cdots & 0 & 0 & 0 & 0 & jE(\omega+\omega_m) & Y_r^{(+2)} & 0 & \cdots \\ \cdots & 0 & 0 & 0 & 0 & 0 & jE(\omega+2\omega_m) & Y_r^{(+3)} & \cdots \\ \iddots & \vdots & \vdots & \vdots & \vdots & \vdots & \vdots & \vdots & \ddots \end{pmatrix}, \quad \textbf{(A4)}$$

where

$$Y_r^{(k)} = jC_0(\omega + k\omega_m) + \frac{1}{jL(\omega + k\omega_m)}\ , \quad \textbf{(A5)}$$

and the coupling among the different harmonics is given by

$$D = \frac{\Delta_m C_0}{2} e^{-j\varphi_m} \text{ and } E = \frac{\Delta_m C_0}{2} e^{+j\varphi_m}. \quad \textbf{(A6)}$$

Furthermore, the coupling between two specific nonlinear harmonics *n* and *k*, with *k*>*n*, can be characterized using admittance inverters as

$$\begin{aligned} J_U^{(k,n)} &= \frac{\Delta_m C_0}{2}(\omega_0 + k\omega_m)e^{j(k-n)\varphi_m} \rightarrow \text{up conversion} \\ J_D^{(n,k)} &= \frac{\Delta_m C_0}{2}(\omega_0 + n\omega_m)e^{j(n-k)\varphi_m} \rightarrow \text{down conversion} \end{aligned} \quad \textbf{(A7)}$$

These expressions explicitly show the nonreciprocal response in amplitude and phase between up/down conversion processes. Besides, they confirm that the coupling between harmonics can be controlled by tailoring the modulation frequency ω_m, the modulation index Δ_m, and the phase φ_m of the modulating signal.

The operation principle of time-modulated resonant unit-cells is as follow. Upon excitation at ω_0, part of the energy is coupled into the cell and is then reflected back without undergoing any frequency conversion. This process yields the standard reflection coefficient [54] that in our formalism is simply obtained by analyzing the incident/reflected waves at the excitation port of the network shown in Fig. A1b. In addition, some energy can be coupled to different nonlinear harmonics and then radiated to free-space, yielding the inter-harmonic reflection coefficients shown in Eq. (2). Such coefficients are computed considering the ratio between the waves at the output port of each harmonic branch of the equivalent electrical network show in Fig. A1b [denoted as $b(\omega_0 + n\omega_m)$] and the incident waves oscillating at the excitation port $a(\omega_0)$. As in the case of networks with several ports, the ports that are not being analyzed should be matched with their corresponding reference impedance.

It should be emphasized that nonreciprocity solely arises due to the nonreciprocal coupling among nonlinear harmonics, as clearly shown in Fig. A1b, which in turn determines the nonreciprocal response of the reflection coefficient. The electromagnetic behavior of any other component of the structure/circuit is reciprocal. Consequently, the nonreciprocal study of time-modulated unit-cells can be reduced to analyzing the coupling among harmonics, as detailed in Eq. (A7), regardless of the cell's complexity.

Appendix B
Numerical simulations

Numerical simulations shown in Fig. 2 were obtained using the commercial package COMSOL Multiphysics. Specifically, we employed a 2D space dimension filled with air and added perfectly matched layers on the left, right, and top sides of the model. To excite the metasurface, we added a "Radio Frequency" physics module to define plane waves oscillating at a desired frequency that impinge onto the metasurface. We included a total of 3 excitation modules corresponding to the frequencies f_0, $f_0 + f_m$ and $f_0 - f_m$. We emphasize that these modules only define the excitation and are not employed to investigate the metasurface response. For each excitation, we incorporated additional "Radio Frequency" physics modules to characterize the linear and harmonic fields scattered by the metasurface. In our case, we analyzed the fields scattered at five frequencies of interest ($f_0, f_0 \pm f_m, f_0 \pm 2f_m$). Therefore, we have a total of 5 "observation" modules per each excitation module. In a given "observation" module, we define the metasurface as a 1D port that couples incoming plane wave defined in an excitation module with the appropriate inter-harmonic gradient reflection coefficients defined in Eq. (4). These numerical simulations provide insight of the phase response and inter-harmonic wavefront capabilities of the proposed metasurface. It should be noted

that the magnitude of each excited harmonic is not included in this type of simulations because it strongly depends on the specific implementation employed to construct the metasurface.

Numerical simulations shown in Fig. 3c were obtained using the commercial software Ansys High Frequency Structure Simulators (HFSS). The unit-cell was excited from the substrate integrated waveguide and periodic boundary conditions were imposed on the free-space. To obtain the results shown in Figs. 4-6, the proposed unit-cell was first simulated in reflection using HFSS as sketched in Fig. 3. In the simulations, tunable capacitors are considered as standard lumped ports. In order to take nonlinear responses into account, the resulting linear scattering matrixes were then analyzed in the commercial software Keysight Advanced Design System (ADS) using the actual model of the lumped components (varactor SMV1232 and inductor LQW18AN5N6D10D, as detailed below) and following the scheme illustrated in Fig. 4a. Similar nonlinear responses can be obtained using the approach detailed in Appendix A instead of ADS. In these numerical simulations, a minimum of 7 nonlinear harmonics were required to achieve convergence.

Numerical simulations shown in Fig. 7-9 are computed using a home-made code based on standard reflectarray/metasurface theory [2-4, 23]. Within this approach, we characterize the electromagnetic response of each unit-cell using measured data from Fig. 4. The analysis of the metasurface in transmission is as follows. First, we assume a standard horn antenna as a feeder and model its radiation pattern using a $cos^q(\theta)$ function [23]. We express the radiated fields in spherical coordinates centered at the feeder position and then derive the fields impinging on each unit-cell of the metasurface. During the last step, we translate the radiated fields to a Cartesian coordinate system, with origin at the metasurface center, using a standard coordinate transformation. Second, we derive the tangential fields induced on the cells. To this purpose, we combine the incoming fields with the scattering parameter matrix of each individual cell. The resulting nonlinear process leads to tangential fields oscillating at different frequencies [23]. And third, we compute the radiation of the fields induced on the entire metasurface using standard techniques [23]. We remark that this approach is commonly used in the field of linear reflectarrays and has been extensively validated with measured data [23]. The approximations employed in this technique are: (i) the variations among adjacent unit-cells are assumed to be negligible, which permits to consider that each unit-cell is within a perfect periodic environment. Such variations appear in common linear reflectarrays because the cells have slightly different geometries. In the proposed configuration, different electromagnetic responses appear because adjacent unit-cells are time-modulated with slightly different phase; (ii) the tangential fields induced on each unit-cell are assumed to be uniform; and (iii) the potential diffraction that might appear at the edges of the metasurface is not considered. The analysis of the metasurface is reception if done using a similar approach.

Appendix C
Description of the fabricated unit-cells and experimental set-up

The fabricated unit-cells are described in Fig. 3. The basic geometry consists of a standard square patch that is coupled through slots to the SIW line (see Fig. C1). The position of the slots with respect to the patch are determined through full-wave simulations to maximize the bandwidth of the cell, as shown in Fig 3c. Substrate 1 (2) is a Roger Corporation laminate RT/duroid 5880 (RO4360G2) with a thickness, permittivity, and tangent loss of h= 1.575 mm (0.406 mm), ε_r= 2.2 (6.15), and tanδ= 0.0009 (0.0038), respectively. Figs. C1a-b provide additional details of the geometry, including the relevant dimensions. Note that the plated via-holes employed to realize the substrate integrated waveguide have a radius of 0.5 mm. A via-hole with a radius of 0.1mm is added close to the end of the SIW connecting the intermediate metal layer to the ground plane. Surrounding the via-hole connection, a circular metallization is added to place two SMV1232 varactors connected back to back in an anti-series configuration that mitigates their nonlinear response and a lumped inductor LQW18AN5N6D10D with 5.6 nH that behaves as a choke. This inductor is connected to a 50 Ω coplanar waveguide printed in the ground plane. We have employed a simple wire (shown in Fig. C1b as a fat black line) to connect the coplanar waveguides inside and outside the regions defined by the via-holes. This configuration clearly separates the radiation and time-modulation mechanisms, avoiding any cross-talk between them.

The details of the experimental set-up employed to characterize the unit-cells are shown in Fig. C1c. Specifically, the board with the cells is placed in an N9911X-210 Keysight waveguide to coaxial flange, as shown in the inset of Fig. 4a. The biasing tone is generated using a signal generator Hewlett Packard E4433B and is then split into two branches using a T-junction. In the upper branch, we have employed the voltage-controlled phase shifter RF-Lambda RVPT0501GBC to manipulate the phase of the signal with a DC voltage source. On the lower branch, we have employed a variable attenuator to provide similar loss as the phase shifter. We have then amplified these signals using identical amplifiers (Hewlett Packard 8347A) and added a DC component to bias the varactors through biasing tees (Picosecond 5530B). These phase-delayed tones are finally applied to time-modulate the unit-cells through their coplanar waveguide port. On the other side of the set-up, we have generated microwave power in the X band using an E8364A Agilent (Keysight) vector network analyzer and directed it towards the WR90 waveguide flange using a directional coupler Krytar 1815. The waves reflected on the unit-cells are then received by a N5247A PNA-X Keysight microwave network analyzer or by an N9030A PXA Keysight signal analyzer, depending on the type of measurement.

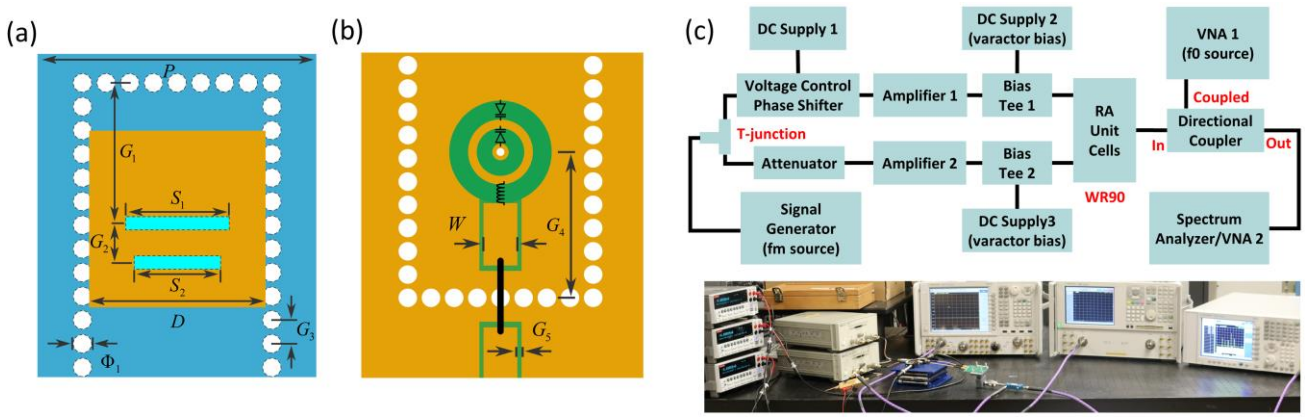

Fig. C1. Details of the intermediate (a) and bottom (b) layers of the fabricated unit-cells (see Fig. 3a) and the experimental set-up (c). Geometrical parameters are P=16.7 mm, D=9.5 mm, S_1=5.8 mm, S_2=5.0 mm, G_1=7.6 mm, G_2=2.4 mm, G_3=1.3 mm, G_4=7.0 mm, G_5=0.2 mm, W=1.8 mm, and Φ_1=1.0 mm The distance between adjacent circumferences shown in panel (b) are 0.5mm, 0.4mm, 0.6mm and 0.5 mm, respectively, starting from the exterior one. The width of both slots is 0.8 mm.

In the experiments shown in Fig. 4 and 5, we have biased the varactors with 6.1 V. The biasing signal f_m carries a total power of 10 dBm, which approximately translates to an amplitude of 1 volt and a modulation index of $\Delta_m = \frac{\Delta C}{C_0} \approx 0.05$, being C_0 the average capacitance and ΔC the maximum capacitance variation from C_0. This value, well in the range of the one employed in other time-modulated devices [43], permits to safely linearize the response of the varactor around the DC biasing point. The response time of the fabricated unit-cell is below 700 ns. In the case of a complete metasurface, taking into account the presence of the feeding lines and the FPGA that controls all unit-cell responses, we estimate a response time under 1 microsecond.

The experimental set-up is calibrated as follows. First, we use the schematic shown in Fig. C1c to excite a uniform piece of copper located in the waveguide with a fixed amount of power. Second, we receive and record the reflected signals across the band of interest, i.e., from 8 to 10 GHz, using the signal analyzer. And third, we employ these signals to normalize all measurement performed with the proposed unit-cells.

References

[1] N. Yu, P. Genevet, M. A. Kats, F. Aieta, J. P. Tetienne, F. Capasso, and Z. Gaburro, Light propagation with phase discontinuities: generalized laws of reflection and refraction, Science **334**, 333 (2011).

[2] N. Yu and F. Capasso, Flat optics with designer metasurfaces, Nat. Mater. **13**, 139 (2014).

[3] A. V. Kildishev, A. Boltasseva, and V. M. Shalaev, Planar photonics with metasurfaces, Science **339**, 1232009 (2013).

[4] N. M. Estakhri and A. Alu, Recent progress in gradient metasurfaces, J. Opt. Soc. Am. B **33**, A21 (2016).

[5] N. M. Estakhri and A. Alu, Wave-front transformation with gradient metasurfaces, Phys. Rev. X **6**, 041008 (2016).

[6] Z. Bomzon, V. Kleiner, and E. Hasman, Pancharatnam–berry phase in space-variant polarization-state manipulations with subwavelength gratings, Opt. Lett. **26**, 1424 (2001).

[7] F. Monticone, N. M. Estakhri, and A. Alu, Full control of nanoscale optical transmission with a composite metascreen, Phys. Rev. Lett. **110**, 203903 (2013).

[8] C. Pfeiffer and A. Grbic, Metamaterial huygens' surfaces: tailoring wave fronts with reflectionless sheets, Phys. Rev. Lett. **110**, 197401 (2013).

[9] C. Pfeiffer and A. Grbic, Millimeter-wave transmitarrays for wavefront and polarization control, IEEE Trans. Microwave Theory Tech. **61**, 4407 (2013).

[10] M. Kim, A. M. H. Wong, and G. V. Eleftheriades, Optical huygens metasurfaces with independent control of the magnitude and phase of the local reflection coefficients, Phys. Rev. X **4**, 041042 (2014).

[11] M. Decker, I. Staude, M. Falkner, J. Dominguez, D. N. Neshev, I. Brener, T. Pertsch, and Y. S. Kivshar, High-efficiency dielectric huygens' surfaces, Adv. Opt. Mater. **3**, 813 (2015).

[12] A. Alu, Mantle cloak: invisibility induced by a surface, Phys. Rev. B **80**, 245115 (2009).

[13] X. Ni, Z. J. Wong, M. Mrejen, Y. Wang, and X. Zhang, An ultrathin invisibility skin cloak for visible light, Science **349**, 1310 (2015).

[14] M. A. Al-Joumayly and N. Behdad, Wideband planar microwave lenses using sub-wavelength spatial phase shifters, IEEE Trans. Antennas Propag. **59**, 4542 (2011).

[15] F. Aieta, P. Genevet, M. A. Kats, N. Yu, R. Blanchard, Z. Gaburro, and F. Capasso, Aberration-free ultrathin flat lenses and axicons at telecom wavelengths based on plasmonic metasurfaces, Nano Lett. **12**, 4932 (2012).

[16] T. Roy, E. T. Rogers, and N. I. Zheludev, Sub-wavelength focusing meta-lens, Opt. Express **21**, 7577 (2013).

[17] N. Engheta, Thin absorbing screens using metamaterial surfaces, IEEE APS Int. Symp. Dig. **2**, 392 (2002).

[18] K. Aydin, V. E. Ferry, R. M. Briggs, and H. A. Atwater, Broadband polarization-independent resonant light absorption using ultrathin plasmonic super absorbers, Nat. Commun. **2**, 517 (2011).

[19] P. Spinelli, M. A. Verschuuren, and A. Polman, Broadband omnidirectional antireflection coating based on subwavelength surface Mie resonators, Nat. Commun. **3**, 692 (2012).

[20] Y. Zhao, M. A. Belkin, and A. Alu, Twisted optical metamaterials for planarized ultrathin broadband circular polarizers, Nat. Commun. **3**, 870 (2012).

[21] C. Pfeiffer and A. Grbic, Cascaded metasurfaces for complete phase and polarization control, Appl. Phys. Lett. **102**, 231116 (2013).

[22] N. Yu, F. Aieta, P. Genevet, M. A. Kats, Z. Gaburro, and F. Capasso, A broadband, background-free quarter-wave plate based on plasmonic metasurfaces, Nano Lett. **12**, 6328 (2012).

[23] J. Huang and J. A. Encinar, *Reflectarray Antennas* (Wiley-IEEE Press, Hoboken, NJ, 2007).

[24] B. A. Munk, *Frequency Selective Surfaces: Theory and Design* (Wiley, New York, 2000).

[25] M. Tymchenko, J. S. Gomez-Diaz, J. Lee, N. Nookala, M. A. Belkin, and A. Alu, Gradient nonlinear pancharatnam-berry metasurfaces, Phys. Rev. Lett. **115**, 207403 (2015).

[26] G. Li, S. Chen, N. Pholchai, B. Reineke, P. W. H. Wong, E. Y. B. Pun, K. W. Cheah, T. Zentgraf, and S. Zhang, Continuous control of the nonlinearity phase for harmonic generations, Nat. Mater. **14**, 607 (2015).

[27] N. Nookala, J. Lee, M. Tymchenko, J. S. Gomez-Diaz, F. Demmerle, G. Boehm, K. Lai, G. Shvets, M.-C. Amann, A. Alu, and M. Belkin, Ultrathin gradient nonlinear metasurface with a giant nonlinear response, Optica **3**, 283 (2016).

[28] Y. Hadad, D. L. Sounas, and A. Alu, Space-time gradient metasurfaces, Phys. Rev. B **92**, 100304(R) (2015).

[29] A. Shaltout, A. Kildishev, and V. Shalaev, Time-varying metasurfaces and Lorentz nonreciprocity, Opt. Mat. Exp. **5**, 2459 (2015).

[30] M. Liu, D. A. Powell, Y. Zarate, and I. V. Shadrivov, Huygens' metadevices for parametric waves, Phys. Rev. X **8**, 031077 (2018).

[31] M. M. Salary, S. Jafar-Zanjani, and H. Mosallaei, Electrically tunable harmonics in time-modulated metasurfaces for wavefront engineering, New J. Phys. **20**, 123023 (2018).

[32] L. Zhang, X. Q. Chen, S. Liu, Q. Zhang, J. Zhao, J. Y. Dai, G. D. Bai, X. Wan, Q. Cheng, G. Castaldi, V. Galdi, and T. J. Cui, Space-time-coding digital metasurfaces, Nat. Commun. **9**, 4334 (2018).

[33] H. B. G. Casimir, On Onsager's principle of microscopic reversibility, Rev. Mod. Phys. **17**, 343 (1945).

[34] C. Caloz, A. Alu, S. Tretyakov, D. Sounas, K. Achouri, and Z. L. Deck-Leger, Electromagnetic nonreciprocity, Phys. Rev. Appl. **10**, 047001 (2018).

[35] Z. Yu and S. Fan, Complete optical isolation created by indirect interband photonic transitions, Nat. Photonics **3**, 91 (2009).

[36] D. L. Sounas, C. Caloz, and A. Alu, Giant non-reciprocity at the subwavelength scale using angular momentum-biased metamaterials, Nat. Commun. **4**, 2407 (2013).

[37] D. L. Sounas and A. Alu, Non-reciprocal photonics based on time modulation, Nat. Photonics **11**, 774 (2017).

[38] Y. Shi, Z. Yu, and S. Fan, Limitations of nonlinear optical isolators due to dynamic reciprocity, Nat. Photonics **9**, 388 (2015).

[39] D. L. Sounas, J. Soric, and A. Alu, Broadband passive isolators based on coupled nonlinear resonances, Nat. Electron. **1**, 113 (2018).

[40] R. Fleury, D. L. Sounas, C. F. Sieck, M. R. Haberman, and A. Alu, Sound isolation and giant linear nonreciprocity in a compact acoustic circulator, Science **343**, 516 (2014).

[41] N. A. Estep, D. L. Sounas, and A. Alu, Magnetless microwave circulators based on spatiotemporally modulated rings of coupled resonators, IEEE Trans. Microwave Theory Tech. **64**, 502 (2016).

[42] D. Correas-Serrano, J. S. Gomez-Diaz, D. L. Sounas, Y. Hadad, A. Alvarez-Melcon, and A. Alu, Nonreciprocal graphene devices and antennas based on spatiotemporal modulation, IEEE Antennas Wireless Propag. Lett. **15**, 1529 (2016).

[43] Y. Hadad, J. C. Soric, and A. Alu, Breaking temporal symmetries for emission and absorption, Proc. Natl. Acad. Sci. U.S.A. **113**, 3471 (2016).

[44] N. Chamanara, S. Taravati, Z. L. Deck-Leger, and C. Caloz, Optical isolation based on space-time engineered asymmetric photonic band gaps, Phys. Rev. B **96**, 155409 (2017).

[45] S. Taravati and C. Caloz, Mixer-duplexer-antenna leaky-wave system based on periodic space-time modulation, IEEE Trans. Antennas Propag. **65**, 442 (2017).

[46] S. Taravati, N. Chamanara, and C. Caloz, Nonreciprocal electromagnetic scattering from a periodically space-time modulated slab and application to a quasisonic isolator, Phys. Rev. B **96**, 165144 (2017).

[47] D. Correas-Serrano, A. Alu, and J. S. Gomez-Diaz, Magnetic-free nonreciprocal photonic platform based on time-modulated graphene capacitors, Phys. Rev. B **98**, 165428 (2018).

[48] X. Wu, X. Liu, M. D. Hickle, D. Peroulis, J. S. Gomez-Diaz, and A. Alvarez Melcon, Isolating bandpass filters using time-modulated resonators, IEEE Trans. Microwave Theory Tech., 2019 (in press), doi: 10.1109/TMTT.2019.2908868.

[49] J. S. Gomez-Diaz, C. Moldovan, S. Capdevila, J. Romeu, L. S. Bernard, A. Magrez, A. M. Ionescu, and J. Perruisseau-Carrier, Self-biased reconfigurable graphene stacks for terahertz plasmonics, Nat. Commun. **6**, 6334 (2015).

[50] A. Woessner, M. B. Lundeberg, Y. Gao, A. Principi, P. Alonso-Gonzalez, M. Carrega, K. Watanabe, T. Taniguchi, G. Vignale, M. Polini, J. Hone, R. Hillenbrand, and F. H. L. Koppens, Highly confined low-loss plasmons in graphene–boron nitride heterostructures, Nat. Mater. **14**, 421 (2015).

[51] M. A. Miri, F. Ruesink, E. Verhagen, and A. Alu, Optical nonreciprocity based on optomechanical coupling, Phys. Rev. Appl. **7**, 064014 (2017).

[52] N. R. Bernier, L. D. Toth, A. Koottandavida, M. A. Ioannou, D. Malz, A. Nunnenkamp, A. K. Feofanov, and T. J. Kippenberg, Nonreciprocal reconfigurable microwave optomechanical circuit, Nat. Commun. **8**, 604 (2017).

[53] C. Coulais, D. Sounas, and A. Alu, Static non-reciprocity in mechanical metamaterials, Nature **542**, 461 (2017).

[54] R. E. Collin, *Foundations for Microwave Engineering*, 2nd ed. (Wiley-IEEE Press, New York, 2001).

[55] A. Nemati, Q. Wang, M. Hong, and J. Teng, Tunable and reconfigurable metasurfaces and metadevices, Opto-Electron. Adv. **1**, 180009 (2018).

[56] S. V. Hum and J. Perruisseau-Carrier, Reconfigurable reflectarrays and array lenses for dynamic antenna beam control: A review, IEEE Trans. Antennas Propag. **62**, 183 (2014).

[57] V. S. Asadchy, M. Albooyeh, S. N. Tcvetkova, A. Diaz-Rubio, Y. Ra'di and S. A. Tretyakov, Perfect control of reflection and refraction using spatially dispersive metasurfaces, Phys. Rev. B **94**, 075142 (2016).

[58] A. Epstein and G. V. Eleftheriades, Synthesis of passive lossless metasurfaces using auxiliary fields for reflectionless beam splitting and perfect reflections, Phys. Rev. Lett. **117**, 256103 (2016).

[59] J. D. Jackson, *Classical Electrodynamics*, 3rd ed. (Wiley, Hoboken, New Jersey, 1999).

[60] M. Bozzi, A. Georgiadis and K. Wu, Review of substrate-integrated waveguide circuits and antennas, IET Microw. Antennas Propag. **5**, 909 (2011).

[61] P. Hannan and M. Balfour, Simulation of a phased-array antenna in waveguide, IEEE Trans. Antennas Propag. **13**, 342 (1965).

[62] R. C. Hansen, *Phased Array Antennas* (John Wiley & Sons, New York, 2009).

[63] C. Kurth, Steady-state analysis of sinusoidal time-variant networks applied to equivalent circuits for transmission networks, IEEE Trans. Circuits Syst. **24**, 610 (1977).